Monocarboxylate-protected two-electron superatomic silver nanoclusters with high photothermal conversion performance

Hao-Hai Wang, Jianyu Wei, Fahime Bigdeli, Farzaneh Rouhani, Hai-Feng Su, Ling-Xiao Wang, Samia Kahlal, J.-F. Halet, Jean-Yves Saillard, Ali Morsali, et al.

Monocarboxylate-Protected Two-Electron *Superatomic* Silver Nanoclusters with High Photothermal Conversion Performance

Hao-Hai Wang,[a†] Jianyu Wei,[a,b†] Fahime Bigdeli,[c†] Farzaneh Rouhani,[c] Hai-Feng Su,[d] Ling-Xiao Wang,[a] Samia Kahlal,[b] Jean-François Halet,[e] Jean-Yves Saillard,*[b] Ali Morsali,*[c] and Kuan-Guan Liu*[a,d]

The first series of monocarboxylate-protected *superatomic* silver nanoclusters was synthesized and fully characterized by X-ray diffraction, Fourier-transform infrared spectroscopy (FT-IR), X-ray photoelectron spectroscopy (XPS) and electrospray ionization mass spectrometry (ESI-MS). Specifically, compounds $[Ag_{16}(L)_8(9\text{-}AnCO_2)_{12}]^{2+}$ (L = Ph_3P (**I**), $(4\text{-}ClPh)_3P$ (**II**), $(2\text{-}furyl)_3P$ (**III**), and Ph_3As (**IV**)) were prepared by using solvent-thermal method under alkaline condition. These clusters exhibit a similar unprecedented structure containing a $[Ag_8@Ag_8]^{6+}$ metal kernel, of which the 2-electron *superatomic* $[Ag_8]^{6+}$ inner core describes a flattened and puckered hexagonal bipyramid of S_6 symmetry. Density functional theory calculations provide a rationalization of the structure and stability of these 2-electron *superatoms*. Results indicate that the *superatomic* 2 electrons occupy a *superatomic* molecular orbital 1S that has a substantial localization on the top and bottom vertices of the bipyramid. The π systems of the anthracenyl groups, as well as the 1S HOMO, are importantly involved in the optical and photothermal behavior of the clusters. The four characterized nanoclusters show high photo-thermal conversion performance of sun light. These results show that the unprecedented use of mono-carboxylates in the stabilization of Ag nanoclusters is possible, opening the door for the introduction of various functional groups on their cluster surface.

1. Introduction

High-nuclearity atom-precise silver nanoclusters (NCs) are currently the subject of intense interest due to their fascinating structures and specific properties[1-7]. Factors such as electronic shell closing, coordination saturation, nature of surface organic ligands, atom packing, and steric hindrance greatly influence the structures, properties, and stability of such NCs[8, 9]. Their structure consists of a metallic kernel, usually exhibiting a core/shell structure, passivated by a protecting ligand shell. Their closed-shell stability is attributed to their magic number of bonding electrons providing from the 5s(Ag) atomic orbitals (AOs). This can be rationalized within the *superatom* concept [10, 11] based on the spherical *jellium* model.[12] It is noteworthy that the ligands are not only acting as stabilizers of the highly reactive cluster metal kernel, but they also significantly influence the properties of the clusters.[13-16]

Silver NCs protected by ligands containing nitrogen and oxygen donor atoms are attracting intense interest due to their unique properties with various potential applications.[8, 17-21] However, according to the hard-soft-acid-base (HSAB) theory,[22-24] preparing a silver cluster with hard base-type ligands such as oxygen-donor ligands is a challenging synthetic process, owing to the rather soft nature of the silver Lewis acid. A series of solutions such as inorganic O-donors (metal oxo or polyoxo) has been developed for the synthesis of these types of O-donors ligand-protected clusters. [25, 26] Using organic O-donors, we recently opened the synthetic route to perfluoroglutarate-protected NCs,[27] and Zang and coworkers developed a series of carboxylate-protected clusters confined in Ti-organic cages[28]. Despite these developments, the use of simple organic O-donor ligands such as mono-carboxylates has not been reported yet. Designing easy methods for the synthesis of mono-carboxylate-protected NCs would render possible the access to a series of species that would benefit from the advantages of carboxylate functional groups, such as availability, affordability and, overall, the huge variety of carboxylate functional groups.[29]

Herein, the synthesis and characterization of a novel series of phosphine- and arsine-mediated monocarboxylate-protected *superatomic* silver NCs are described. These new molecular models show high photothermal response. It is noteworthy that photothermal materials based on silver NCs have been shown to be good candidates to efficiently convert light into heat by increasing the solar energy absorption in the high-energy region[30]. Thus, such systems constitute good models for understanding the photothermal conversion mechanisms at the molecular level[5, 6]. In our compounds, a bulky monocarboxylic acid (9-anthracene carboxylic acid) as a protecting agent was used. The choice of such carboxylate ligands originates from their multi-ring aromatic π-system that has been widely used as UV absorbers[31, 32], photosensitizers[33, 34] or transmitters[20] for their sensitization and great absorption of the short wavelength irradiation[21] to improve their ability in optical absorption. Moreover, the presence of free electrons in the core of these *superatomic* species can promote a bathochromic shift in the absorption of long wavelength irradiation,[35, 36] favoring photothermal efficiency.

2. Experimental Section

2.1 Synthesis of the nanoclusters

The general method used for the synthesis of the **I**-**IV** NCs is described in Scheme 1.

Synthesis of $[Ag_{16}(Ph_3P)_8(9\text{-}AnCO_2)_{12}](OH)_2$ (I·$(OH)_2$): 9-Anthracene carboxylic acid (0.067 g, 0.3 mmol) was added to a solution of $AgNO_3$ (0.051 g, 0.3 mmol) or AgOTf (OTf: trifluoromethanesulfonate) (0.077 g, 0.3 mmol) in methanol (CH_3OH, 6 mL) under ultrasonication. 42 µL of triethylamine (TEA), 0.3 mmol) and 0.026 g (0.1 mmol) of Ph_3P were added to the resulting muddy solution, successively, which was still muddy. Then 2 mL of dimethyl formamide (DMF) were added. A cloudy solution was obtained after ultrasound treatment. The reaction mixture was sealed and kept at 70 ℃ for 20 h. After cooling to room temperature, yellow block

crystals of **I·(OH)$_2$** were obtained. *Anal. Calcd* for NC **I·(OH)$_2$**: $C_{324}H_{230}O_{26}P_8Ag_{16}$: C, 59.75; H, 3.56. Found: C, 60.03; H, 3.91.

Synthesis of {Ag$_{16}$[(4-ClPh)$_3$P]$_8$(9-AnCO$_2$)$_{12}$}(OH)$_2$ (II·(OH)$_2$): 9-Anthracene carboxylic acid (0.067 g, 0.3 mmol) was added to a solution of $AgNO_3$ (0.051 g, 0.3 mmol) or AgOTf (0.077 g, 0.3 mmol) in acetonitrile (CH_3CN, 6 mL) under ultrasonication. 42 µL of TEA (0.3 mmol) and 0.026 g (0.1 mmol) of $(4\text{-ClPh})_3P$ were added to the resulting muddy solution, successively, which was still muddy. Then 1 mL of DMF was added. A cloudy solution was obtained after ultrasound treatment. The reaction mixture was sealed and kept at 70 ℃ for 20 h. After cooling to room temperature, yellow block crystals of **II·(OH)$_2$** were obtained. It is noteworthy that when using 2 mL of DMF solvent cluster **II·(OH)$_2$** could not be obtained and we

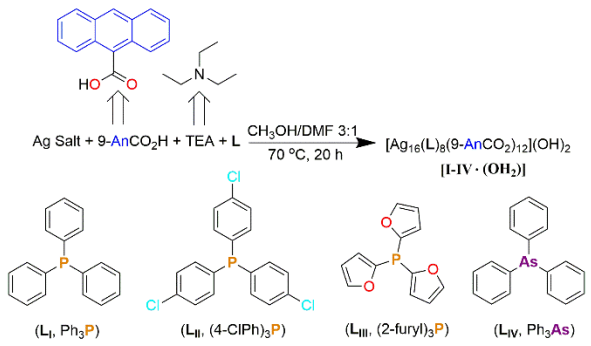

Scheme 1 The synthetic routes of crystals **I-IV·(OH)$_2$**.

think this is related to the different solubilities of the phosphines in the reaction system. *Anal. Calcd* for NC **II·(OH)$_2$**: $C_{324}H_{206}O_{26}P_4Cl_{24}Ag_{16}$: C, 53.93; H, 2.88. Found: C, 54.23; H, 3.92.

Synthesis of {Ag$_{16}$[(2-furyl)$_3$P]$_8$(9-AnCO$_2$)$_{12}$}(OH)$_2$ (III·(OH)$_2$): 9-Anthracene carboxylic acid (0.067 g, 0.3 mmol) was added to a solution of AgOTf (0.077 g, 0.3 mmol) in methanol (6 mL) corrections[47] were employed in order to take into account dispersion effects. Because of computational limitations, natural atomic orbital (NAO) populations were calculated with the Gaussian16 package[48] via its NBO3.1 module,[49] by using the ADF optimized geometries with a Def2-SVP basis[50] set and BP86 functional. In order to reduce computational efforts, the Gaussian16 package was also used for calculating the UV-Vis optical transitions by time-dependent DFT (TD-DFT) at the Def2-SVP/PBE0[51] level of theory.

3. Results and Discussion

3.1 Structure Description

The clusters **I-IV·(OH)$_2$** were prepared by using a similar solvent-thermal method, as reported in our previous work, under the alkaline condition.[19] TEA was used as both a base source and a (weak) reductant.[52, 53] The structures of clusters **I-IV** were characterized by single-crystal X-ray diffraction (Table S1). Clusters **I** and **IV** crystallize in the cubic $Pa\bar{3}$ space group, whereas clusters **II** and **III** crystallize in the trigonal $R\bar{3}$ group. Based on these results, the general formula of **I-IV** is: $[Ag_{16}(L)_8(9\text{-AnCO}_2)_{12}]^{2+}$ (L = Ph_3P (**I**), $(4\text{-ClPh})_3P$ (**II**), $(2\text{-furyl})_3P$ (**III**), Ph_3As (**IV**)). The presence of two hydroxide anions in the formula could originate from the use of imperfectly dried solvent. The dicationic nature of the clusters $[Ag_{16}(L)_8(9\text{-AnCO}_2)_{12}]^{2+}$ was also confirmed by ESI-MS (see below). In the crystal, they all adopt the same structure of perfect S_6 symmetry with a unique Ag_8@Ag_8 core-shell arrangement (Figure 1). The eight inner silver atoms (purple) describe a flattened hexagonal bipyramid, with the hexagonal base somewhat chair-distorted. The S_6 symmetry axis passes through the top and bottom vertices of the bipyramid (Figures 1 and S1), which are in close contact (~2.7 Å) with each other. All but one of the bipyramid edge lengths are lower than 2.9 Å (Table S2), indicating some degree of covalency. Alternatively, the Ag_8 inner core can also be seen as forming a parallelepiped or compressed rhombohedron. Each of the eight inner silver atoms is bonded to three carboxylate oxygen atoms in a pyramidal fashion. The eight outer Ag atoms (green) lie on the top of each inner Ag atoms, but they are not in contact with them or with any other metal center (Ag…Ag > 3.4 Å). They are only bonded to ligands. The six outer silver atoms surrounding the puckered hexagonal base of the Ag_8 bipyramid are bonded to one L ligand and two carboxylate oxygen atoms in a nearly planar tri-coordination mode. The two other outer silver atoms that lie on the S_6 axis are bonded to one L ligand and three oxygen atoms in a tetrahedral fashion. Based on the silver-ligand interactions above described, two kinds of new surface motifs (Figure 2a and 2c) can be distinguished. The first one (Figure 2a) consists of a $[(L)Ag(9\text{-AnCO}_2)]_6$ "hexamer" surrounding the hexagonal base of the Ag_8 bipyramid and composed of the six tri-coordinated outer silver atoms, six phosphines or arsines, and six μ_4-η^2_{trans},η^2_{trans} anthracene-9-carboxylates. The second one (Figure 2c) is a $[(L)Ag(9\text{-AnCO}_2)_3]$ triangular "tie" located at the top and bottom of the Ag_8 bipyramid and composed of one tetrahedrally coordinated outer silver atom, one phosphine or arsine, and three μ_4-η^2_{trans},η^2_{cis} anthracene-9-carboxylates.

The carboxylate ligands being monoanionic, one is left with a formally $[Ag_{16}]^{14+}$ core in $[Ag_{16}(L)_8(9\text{-AnCO}_2)_{12}]^{2+}$. Owing to the fact that the eight outer Ag atoms are isolated from any of their congeners, one is led to consider them as in a +I oxidation state, making locally stable planar-tri-coordinated 16-electron (for six of them) and tetrahedrally coordinated 18-electron (for two of them) metal centers, respectively. Thus, one is left with an $[Ag_8]^{6+}$ core, which, with two delocalized (so-called free) electrons originating from the two formally occupied 5s(Ag) atomic orbitals (AOs), can be viewed as a closed-shell 2-electron *superatom* of $1S^2$ configuration.[54] Note that a 2-electron bicapped octahedral (or rhombohedral) $[Ag_8]^{6+}$ NC core is also known, [19] as well as a tetracapped tetrahedral $[Ag_8]^{6+}$ NC core.[28] However, a new $[Ag_8]^{6+}$ polyhedral architecture is spotted here for the first time. Its mixed-valent nature is consistent with the fact that most of the Ag…Ag contacts (Table S2) are shorter than that 'argentophilic' interactions (2.8 Å),[55] similarly as in many other mixed-valent silver NCs[18, 56, 57]. The FT-IR spectra, as well as the recorded and simulated powder XRD patterns of these NCs are consistent with their single-crystal X-ray structure (Figures S2 and S3). It should also be minded that a related hexagonal bipyramidal structure has been shown to be adopted by a series of 2-electron $[Au_2Cu_6L_2(SR_6)]$ (L = phosphine) clusters.[58, 59] However, this structure differs from ours by the planarity of the Cu_6 hexagonal base (the Au_2Cu_6 core is of D_{3h} symmetry) and by the very different coordination modes of the ligands. To finish this structural analysis of the cluster core, one should notice that there is a continuous

pathway which connects the above-mentioned D_{6h} hexagonal bipyramid to the D_{3d} bicapped octahedral arrangement adopted by the $[Ag_8]^{6+}$ core of $[Ag_8(pfga)_6]^{6-}$ (pfga = perfluoroglutatate)[19]. It turns out that the $[Ag_8]^{6+}$ inner core of clusters **I-IV** adopts one of the intermediate structures of S_6 symmetry that connect these two geometrical limits.

under ultrasonication. 42 µL of TEA (0.3 mmol) and 0.023 g (0.1 mmol) of (2-furyl)$_3$P were added to the resulting muddy solution, successively, which was still muddy. Then 2 mL of DMF were added. A cloudy solution was obtained after ultrasound treatment. The reaction mixture was sealed and kept at 70 ℃ for 20 h. After cooling to room temperature, yellow block crystals of **III·(OH)$_2$** were obtained. *Anal. Calcd* for NC **III·(OH)$_2$**: $C_{276}H_{178}O_{56}P_8Ag_{16}$: C, 52.09; H, 2.82. Found: C, 52.38; H, 2.98.

Synthesis of $[Ag_{16}(Ph_3As)_8(9\text{-}AnCO_2)_{12}](OH)_2$ (IV·(OH)$_2$): 9-Anthracene carboxylic acid (0.067 g, 0.3 mmol) was added to a solution of AgOTf (0.077 g, 0.3 mmol) in methanol (6 mL) under ultrasonication. 42 µL of TEA (0.3 mmol) and 0.031 g (0.1 mmol) of Ph_3As were added to the resulting muddy solution, successively, which was still muddy. Then 2 mL of DMF were added. A cloudy solution was obtained after ultrasound treatment. The reaction mixture was sealed and kept at 70 ℃ for 20 h. After cooling to room temperature, yellow block crystals of **IV·(OH)$_2$** were obtained. *Anal. Calcd* for NC **IV·(OH)$_2$**: $C_{324}H_{230}O_{26}As_8Ag_{16}$: C, 56.69; H, 3.38. Found: C, 56.74; H, 3.66

2.2 X-ray Structure Analysis

X-ray-quality crystals of the clusters **I-IV·(OH)$_2$** were directly obtained by solvothermal method, and X-ray crystallographic data were recorded at 154 K for **I·(OH)$_2$**, 159 K for **II·(OH)$_2$**, 293 K for **III·(OH)$_2$**, 193 K for **IV·(OH)$_2$** by mounting a single-crystal of clusters **I·(OH)$_2$** (0.21 ×0.15 ×0.07 mm^3), **II·(OH)$_2$** (0.07 ×0.06 ×0.06 mm^3), **III·(OH)$_2$** (0.06 ×0.05 ×0.04 mm^3), and **IV·(OH)$_2$** (0.22 ×0.17 ×0.09 mm^3), respectively. Intensity data of the NCs were collected on a Bruker SMART APEX CCD diffractometer (Mo Kα source for **I·(OH)$_2$**, **II·(OH)$_2$**, **IV·(OH)$_2$**; Cu Kα source for **III·(OH)$_2$**). Absorption corrections were applied by using the program CrysAlis (multi-scan). The structures were solved by direct methods, and all non-hydrogen atoms were refined anisotropically by least-squares on F^2 using the SHELXTL program[1-6, 30, 37-39]. The hydrogen atoms of the organic moieties were generated geometrically.

2.3 Photothermal Experiments

A Xenon lamp (300 W) was used as the light source to simulate the solar irradiation during the photo-thermal conversion experiments (by using an AM 1.5 G optical filter, with light intensity 0.1 W•cm^{-2}). The sample was placed in a 2.0×2.0 cm^2 glass sample cell right under the light source (30 cm). The sample surface temperature changes with time recorded by FLIR infrared thermography. The test conditions were performed under ambient temperature (29 ℃) and humidity (30 %). The photothermal conversion efficiency was calculated according to a previous method.[40]

2.4 Other Analyses and Characterization

Microanalyses of C, H, and N were carried out with a CE instruments EA 1110 elemental analyzer. IR spectra were recorded from KBr pellets in the range 4000-400 cm^{-1} with a Nicolet AVATAR FT-IR330 spectrometer. Emission spectra were measured on a Hitachi F-7000 spectrometer. UV/Vis absorption spectra were measured on a SHIMADZU UV2550 spectrophotometer. Luminescence, lifetime and quantum yield (solid state) were measured on an Edinburgh FLS980 apparatus. ESI-MS was performed on an Agilent Technologies ESI-TOF-MS spectrometer. Qualitative analysis was carried out using GCMS-QP2010 Plus with EI ion source, EI-MS standard database, and an RTX-5 quartz capillary column. X-ray photoelectron spectroscopy (XPS) studies were performed on PHI Quantum-2000 XPS. The sample was put under UHV to reach the 10^{-8} Pa range. The non-monochromatized Al Kα source was used at 10 kV and 10 mA. All binding energies were calibrated using the C (1s) carbon peak (284.6 eV), which was applied as an internal standard. High resolution narrow-scan spectra were recorded with the electron pass energy of 50 eV and takeoff angle of 55° to achieve the maximum spectral resolution.

2.5 Computational Details

Geometry optimizations were carried out within the density functional theory (DFT) formalism using the ADF2018 code.[41, 42] Scalar relativistic corrections via the ZORA Hamiltonian[43] were included together with the Becke-Perdew (BP86) functional.[44, 45] A triple-ξ Slater basis set plus a polarization function (TZP) was used.[46] The frozen core approximation was applied to the [1s^2-4p^6] shells for Ag, [1s^2-2p^6] for P, and [1s^2] for C and O, leaving the remaining electrons to be treated variationally. Grimme's DFT-D3 empirical

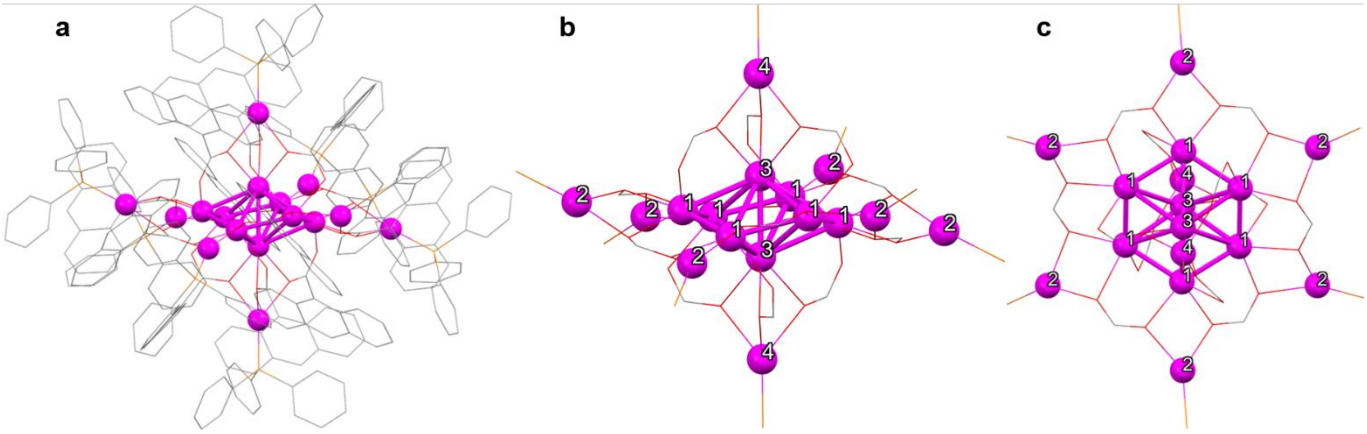

Fig. 1 The full structure (a), side view (b) and top view (c) of $[Ag_{16}(\mathbf{L})_8(9\text{-}AnCO_2)_{12}]^{2+}$ [**L** = Ph_3P (**I**); $(4\text{-}ClPh)_3P$ (**II**); $(2\text{-}furyl)_3P$ (**III**); Ph_3As (**IV**)]. Color code: grey ball, grey stick, red stick and orange stick represent Ag, C, O and P (or As), respectively. H atoms are omitted for clarity.

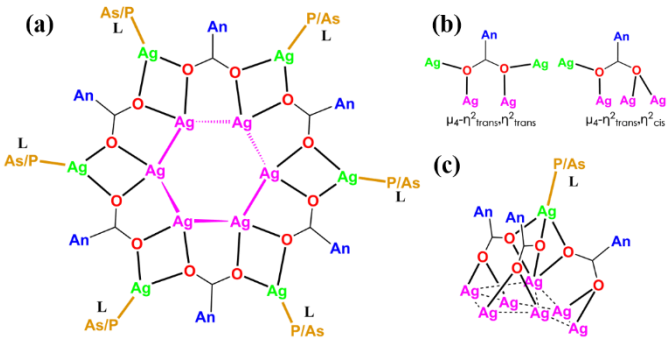

Fig. 2 Two different binding motifs of the monocarboxylates: (a) the [(**L**)Ag(9-$AnCO_2$)]$_6$ hexamer, (b) the schematic representation of the surface motifs: and (c) the triangular "tie" [(**L**)Ag(9-$AnCO_2$)$_3$]. Color code: green, surface Ag; purple, inner Ag.

3.2 Mass Spectrometry and X-ray Photoelectron Spectroscopy Analysis

The charge state and chemical composition of cluster **IV** were determined by positive-ion ESI-MS. Its spectrum in CH_3OH solution is shown in Figure 3. It has three dominant peaks (**A**, **B** and **C**). The prominent peak **A** centred at m/z = 3472.31 is ascribed to [**M** + H_2O + $3CH_3OH]^{2+}$ (calculated m/z = 3472.31) with **M** = $[Ag_{16}(Ph_3As)_8(9\text{-}AnCO_2)_{12}]$. Peak **B** centred at m/z = 3424.21 and peak **C** centred at *m/z* = 3307.33 are assigned to the [**M** + $H_2O]^{2+}$ (calculated m/z = 3424.28) and [**M** - $2Ag^0]^{2+}$ (calculated m/z = 3307.40) formulae, respectively (Figure S4). Overall, the ESI-MS spectra confirmed **M**= $[Ag_{16}(Ph_3As)_8(9\text{-}AnCO_2)_{12}]$ as a dication. The high-resolution XPS spectrum further confirmed the mixed-valent nature of the clusters (Figure S5). The Ag $3d_{5/2}$ XPS peak was deconvoluted into two peaks with the almost one-to-seven ratio of Ag^0 to Ag^+ (Figures 4 and S5).[27]

3.3 Optical Properties

For further understanding the light absorption mechanism of NCs **I**-**IV**,[60] their optical features were investigated. Their solid-state UV-Vis spectra show strong and multiple absorption bands in the 200-500 nm range, suggesting good absorption upon short wavelength irradiation (Figure S6a). Their optical HOMO-LUMO gaps were estimated from the onset of these spectra (Figure S6b) (**I**: 2.34 eV, **II**: 2.56 eV, **III**: 2.33 eV, **IV**: 2.40 eV). They indicate negligible effect of the phosphine (or arsine) nature. Their UV-vis absorption spectra in DMF show two distinct peaks at 3.28 eV (α; 378 nm, ε_{max} = 5.5×10^4 L·mol^{-1}cm^{-1}) and 4.71 eV (β; 263 nm, ε_{max} = 9.2×10^4 L·mol^{-1}cm^{-1}) (Figure 5) that are consistent with the simulated spectra obtained from time-dependent density functional theory (TD-DFT) calculations (see below).

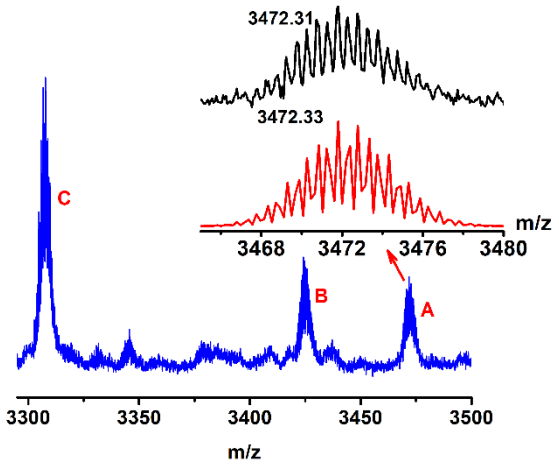

Fig. 3 Positive-ion mode ESI-MS of the crystal **IV** of **M** = $[Ag_{16}(Ph_3As)_8(9\text{-}AnCO_2)_{12}]$ dissolved in CH_3OH. Inset: Zoom-in ESI-MS of the experimental (black line) and simulated (red line) isotopic patterns for species **A** = $[\mathbf{M}+H_2O+3CH_3OH]^{2+}$ at 3472.31.

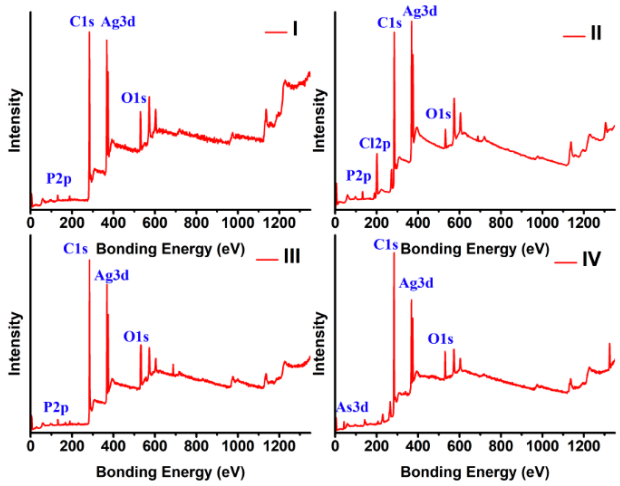

Fig. 4 XPS spectra of nanocluster **I**.

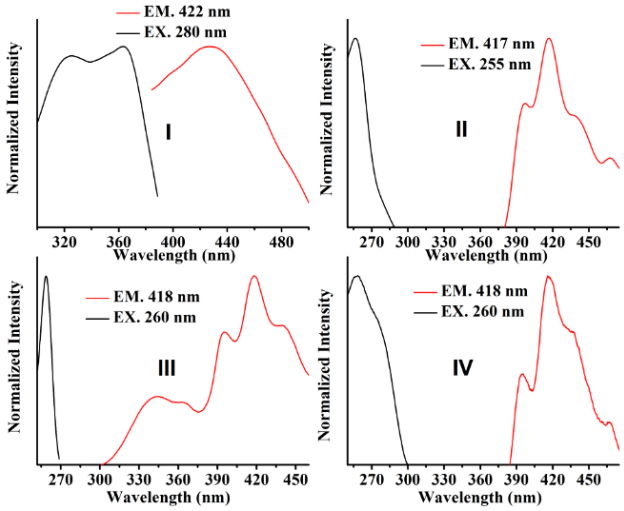

Fig. 6 Photoluminescence analysis of nanoclusters **I-IV** in the solid state at room temperature.

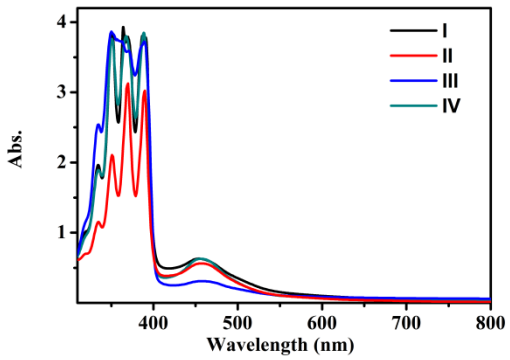

Fig. 5 UV-vis absorption spectra of nanoclusters **I-IV** in the DMF solution

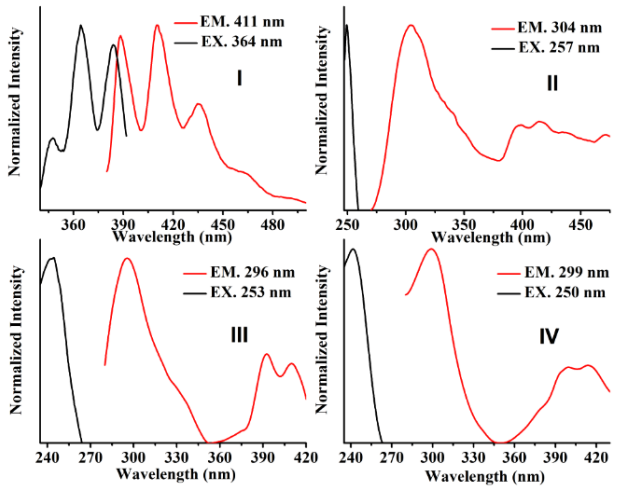

Fig. 7 Photoluminescence analysis of nanoclusters **I-IV** in the solid state at 77K.

The photoluminescence properties of clusters **I-IV** were also investigated in the solid state. At room temperature, the emission (fluorescence) spectra show a major peak around 420 nm (Figure 6). At 77 K, the peak around 420 nm is still present, but in the case of compounds **II-IV** a more intense peak appears around 300 nm (Figure 7). It is noteworthy that the free ligand in its acidic form 9-AnCOOH fluoresces at 466 nm at room temperature in CH_2Cl_2 solution.

3.4 Photo-thermal Conversion Properties

Considering the efficient UV-vis absorption properties of clusters **I-IV**, with the conjugated aromatic anthracene group over the ligand sphere, potential photothermal conversion properties are expected for these compounds.[61] Indeed, the carboxylate ligands, which contain multiple aromatic rings, can strongly absorb light, and on the other hand, the silver core with unique electrical properties and special heat capacity is well suited for converting light into heat[30]. To accurately evaluate the photothermal conversion performance of the four NCs, the cluster powder was fixed on a piece of quartz glass to form a uniform film. The photothermal conversion properties of the four NCs were conducted with simulated sunlight absorption. The temperature of all the NC samples increased rapidly under 1-sun irradiation (0.1 W•cm^{-2}, 420–780 nm), as confirmed by an IR camera. As shown in Figure 8, when the light was turned on, the temperature of **I-IV** rises rapidly to a maximum of 81.6 ℃, 72.3 ℃, 70.4 ℃, 70.3 ℃ in 20 min (Figure S7), increasing by 58.5 ℃, 37.5 ℃, 38.6 ℃, 38.6 ℃, respectively. Then the NC samples reached a quasi-steady-state, over the next 40 min, the temperature increasing by only 0.5~2.9 ℃ (Figure 8). To confirm the role of the components in photothermal effect, a set of control experiments, including the background (quartz

glass), the metal precursors (AgOTf) and the 9-Anthracene carboxylic acid ligand, were performed (Figure S8). After 1 h irradiation, the temperatures of the background, AgOTf and 9-AnCOOH ligand increased only by 18.8 ºC, 20.5 ºC and 22.4 ºC, indicating that the observed high photothermal performance is mainly derived from the photothermal effect of the NCs. The photothermal conversion efficiency of these NCs can be calculated from their cooling curves[62] (See Figure S9), the obtained conversion efficiencies for I-IV are 41.1 %, 35.8 %, 40.7 % and 33.6 %, respectively. In addition, the I-IV samples could be re-used for four photothermal cycles without any inactivation, suggesting excellent stability and photothermal recyclability (Figure S10). Moreover, the XRD patterns of these cluster samples after four photothermal cycles confirms their structural stability (Figure S11), except for cluster II, which partially decomposes to Ag_2O after four photothermal cycles (Figure S11). Owing to the existence of multiple π-delocalized anthracene groups on the cluster surface and that of free electrons within the $[Ag_8]^{6+}$ core, an efficient intramolecular charge transfer is expected to enhance light absorption[38, 63, 64], followed by a ligand-to-metal charge transfer (LMCT) which quenches the photon re-emission process, thus favouring the photothermal conversion. This light-induced LMCT is confirmed by DFT calculations (see below). Compared to other silver-based photothermal materials, clusters I-IV show the best temperature increment under 1-sun (0.1 W•cm^2) by far.[65] Our results suggest that Ag clusters can be efficient candidates in various photothermal applications, for instance photothermal anti-counterfeiting[66], photothermal water evaporation[67], solar thermoelectric production[68-72], etc., strongly encouraging further exploration of the Ag NC chemistry in this direction.

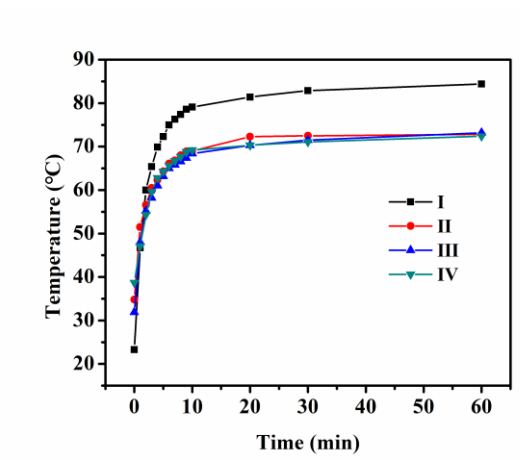

Fig. 8 Temperature variation curves of nanoclusters **I-IV**.

3.5 Computational Analyses

DFT calculations at the ZORA-BP86/TZP/D3(BJ) level were performed on cluster **I** (see Computational Details). The ideal symmetry of **I** is S_6, but its fully optimized geometry was found to be slightly distorted (C_i). Relevant computed data are provided in Table 1 and its Kohn-Sham MO diagram is shown in Figure 9a. The large computed HOMO-LUMO gap (1.70 eV) is consistent with cluster stability. The MO diagram also indicates that no other closed-shell electron counts are possible for such a structure, confirming the dicationic nature of **I**. The optimized Ag-Ag distances within the Ag_8 inner core, ranging from 2.698 Å to 2.994 Å, are consistent with their experimental X-ray counterparts. The HOMO of **I** shows a significant localization on the inner Ag_8 core (with 5s/5p participation) and can be identified as the *superatomic* 1S orbital, with a sizable participation of the ligand (An) shell. The six lowest unoccupied molecular orbitals show major ligand (π*(An)) character. The LUMO+6 and LUMO+7, which contain large 5s/5p(Ag) character, can be easily identified as the *superatomic* $1P_x$ and $1P_y$ orbitals. Owing to the oblate (flattened) nature of the cluster, the $1P_z$ orbital is destabilized at substantially higher energy and is not shown in this diagram. Thus, **I** can be considered as a 2-electron *superatom* with $1S^2$ configuration. The preferred localization of the 1S HOMO on the Ag_8 inner core and the computed NAO charges (Table 1) confirm the $\{[Ag_8]^{6+}\}@\{(Ag^+)_8\}$ charge partitioning suggested in the structural analysis above. The non-spherical nature of the $[Ag_8]^{6+}$ core is not uncommon for 2-electron *superatoms*,[27, 28, 73-82] providing it is compact enough to give the full in-phase 1S orbital a sufficiently bonding character. This strong anisotropy of the S_6 inner core induces a neat differentiation of its two types of symmetry-equivalent vertices, which is reflected by their different charges and configurations (Table 1). Obviously, the two free electrons are substantially more localized on the Ag_{cap} atoms (top and bottom of the bipyramid) rather than on those constituting the chair-distorted hexagonal base of the bipyramid (Ag_{hex}). A similar result was computed for the bare (unligated) $[Ag_8]^{6+}$ fragment. Stretching to the limit our formal charge partitioning, the $[Ag_8]^{6+}$ inner core of **I** could be described as a neutral $(Ag_{cap})_2$ dimer surrounded by a crown of six Ag_{hex}^+ ions. This extreme view is however at least in part contradicted by the computed Ag_{hex}-Ag_{hex} Wiberg bond index (Table 1), which, when compared to its Ag_{cap}-Ag_{cap} counterpart, is consistent with non-negligible (although weak) covalency, thus indicating some delocalization of the free electrons on the Ag_{hex} centers. In any case, the marked difference between Ag_{cap} and Ag_{hex} is consistent with the fact the high-resolution XPS spectra of **I-IV** can be resolved into two peaks, tentatively assigned to Ag(0) and Ag(I) in an approximate one-to-seven ratio, respectively (see above). We suggest that these experiments could not distinguish the six Ag_{hex} core atoms, which bear a minor part of the free electrons, from the outer Ag(I) ones.

It is of note that calculations carried out with simplified phosphine and/or carboxylic ligands yielded geometries that are different from those found for the clusters. Therefore, the specific architecture of clusters **I-IV** is the result of a compromise between ligand steric hindrance, metal/ligand charge equilibrium and metal-metal bonding. This compromise results in a cluster bearing a dicationic charge, which in turn seeks for two hydroxide counterions from water traces in the solvent.

Table 1 Relevant computed data for **I** (averaged to S_6). X-ray-measured distances are reported for comparison.

		DFT	X-ray
Atomic distances (Å) and WBIs[a]	Ag_{cap}-Ag_{cap} (inner core)	2.708 [0.331]	2.753
	Ag_{cap}-Ag_{hexa} (inner core)	3.092 [0.156]	3.131
		2.895 [0.161]	2.852
	Ag_{hexa}-Ag_{hexa} (inner core)	2.698 [0.111]	2.711
	Ag_{inner}...Ag_{outer}	3.520 [0.067]	3.598
	Ag-O	2.417 [0.112]	2.400
	Ag-P	2.323 [0.394]	2.355
HOMO-LUMO gap		1.70 (eV)	
NAO charges and electronic configurations	2 × Ag_{cap} (inner core)	-0.09	
		$4d^{9.87}\ 5s^{0.37}\ 5p^{0.85}$	
	6 × Ag_{hexa} (inner core)	+0.35	
		$4d^{9.90}\ 5s^{0.19}\ 5p^{0.57}$	
	8 × Ag_{outer} (av.)	+0.60	
		$4d^{9.86}\ 5s^{0.30}\ 5p^{0.24}$	

[a] In brackets.

The TD-DFT-simulated UV-vis spectrum of **I** (Figure 9b) is in a good agreement with its experimental counterpart (Figure 5). The experimental weaker absorption band at 460 nm and the four absorption bands between 350 nm and 400 nm are well reproduced, with a reasonably small red shift in the high energy region (one peak at 448 nm and two peaks at 413 nm and 396 nm). A detailed frontier orbital analysis in Figure 9c shows that the transitions associated with the absorption band at 448 nm are from the ligand-type (mainly π(An)) HOMO-4 orbital to the mixed metal/ligand-type LUMO and to the two *superatomic* 1P levels (LUMO+6, LUMO+7), thus of LMCT major character. The more intense bands are associated with several transitions that are of major LLCT character (anthracenyl π→π* essentially).

Owing to the particularly large size of the cluster, it was not possible for us to calculate by TD-DFT the fluorescence emission wavelength corresponding to the transition from the first excited singlet state to the ground state. On the other hand, such calculations were performed on the free ligand 9-AnCOOH, for which the value computed at the same level of theory is 477 nm, a value close to the room-temperature experimental counterpart (466 nm, see above) and not much different from those recorded for clusters **I**-**IV** (~ 420nm), suggesting that the emissive behavior of the clusters is ligand (π*→π) in nature. Another computed emission with large oscillator strength was computed at 274 nm. It is close to that observed at low temperature for clusters **II**-**IV** (see above). One can therefore conclude that the weak emissive behavior of clusters **I**-**IV** is to be associated with that of their An substituents. This is consistent with the hypothesis that the photothermal behavior consists in a ligand (π*(An)) to metal (1S HOMO) non-radiative deactivation.

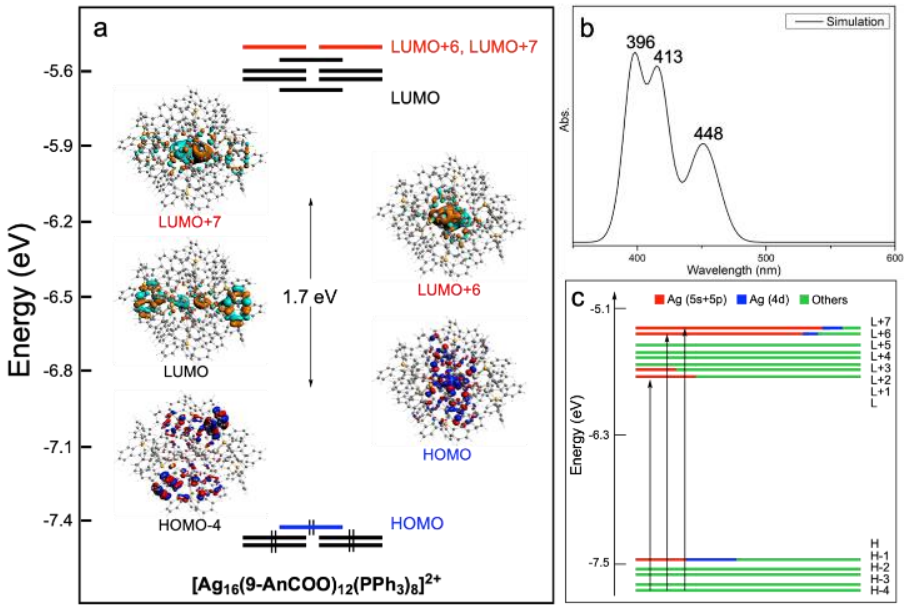

Fig. 9 (a) Kohn-Sham MO diagram of **I** . The blue and red levels correspond to the *superatomic* 1S and 1P levels, respectively. (b) The simulated UV-vis spectra of **I** obtained from TD-DFT calculations. (c) Frontier MO composition and electronic transitions associated with the main absorption bands.

4. Conclusion

In summary, the first monocarboxylate-protected *superatomic* silver NCs $[Ag_{16}(L)_8(9\text{-}AnCO_2)_{12}]^{2+}$ (L = phosphine or arsine) were isolated and fully characterized for the first time. These 2-electron heteroleptic species feature an $[Ag_8@Ag_8]^{14+}$ core-shell structure, with a $[Ag_8]^{6+}$ *superatomic* inner core, adopting an unprecedented structure that describes a distorted hexagonal bipyramidal structure of S_6 symmetry, whereas the outer Ag_8 shell is made of the unique "$Ag(PR_3)$-AnCOO-$Ag(PR_3)$" staple motifs. DFT calculations indicate

that the two free electrons are preponderantly located on the top and bottom atoms of the bipyramid, approaching a dimeric Ag_2 state. The NC surface also exhibits unprecedented structural features, formed by the original arrangement of eight outer Ag^+, monocarboxylates and phosphines/arsines. DFT calculations show also that these distinctive architectures are due, not only to their electron count, but also to the nature and steric hindrance of the carboxylate ligands, which is very rare so far. The investigated NCs show excellent photothermal conversion ability, so far overpassing other silver-based photothermal materials. TD-DFT calculations suggest that this striking property is associated with the existence of multiple π-delocalized anthracene groups on the cluster surface and that of two free electrons within the $[Ag_8]^{6+}$ core. Because of the wide availability and variability of monocarboxylic acids, this work could pave the way for the synthesis of new monocarboxylate-protected coinage metal NCs with larger metal kernels and with various functionalized carboxylates for the design of NCs with desired properties.

Author Contributions

The manuscript was written through contributions of all authors.

Conflicts of interest

The authors declare no competing financial interest.

Acknowledgements

The experimental work was supported by the National Natural Science Foundation of China (Grant No. 92161106), the Natural Science Foundation of Ningxia (Grant No. 2022AAC05017), the Foundation of State Key Laboratory of Physical Chemistry of Solid Surfaces (Grant No. 202013) and Tarbiat Modares University. We are extremely grateful to Wenyan Dan of Tongji University for his help with the crystal structure determination. The Grand Equipment National de Calcul Intensif is acknowledged for HCP support (Project a0010807367).

Notes and references

1 K.-G. Liu, F. Bigdeli, H.-J. Li, J.-Z. Li, X.-W. Yan, M.-L. Hu and A. Morsali, *Inorg. Chem.*, 2020, **59**, 6684.
2 J.-W. Liu, H.-F. Su, Z. Wang, Y.-A. Li, Q.-Q. Zhao, X.-P. Wang, C.-H. Tung, D. Sun and L.-S. Zheng, *Chem. Commun.*, 2018, **54**, 4461.
3 M. S. Bootharaju, G. K. Deepesh, T. Udayabhaskararao and T. Pradeep, *J. Mater. Chem. A*, 2013, **1**, 611.
4 D. Jonckheere, E. Coutino-Gonzalez, W. Baekelant, B. Bueken, H. Reinsch, I. Stassen, O. Fenwick, F. Richard, P. Samorì, R. Ameloot, J. Hofkens, M. B. J. Roeffaers and D. E. De Vos, *J. Mater. Chem. C*, 2016, **4**, 4259.
5 K. Mikami, H. Shen, K. Kubo, S. Kume and T. Mizuta, *Dalton Trans.*, 2021, **50**, 5659.
6 B. Li, R.-W. Huang, J.-H. Qin, S.-Q. Zang, G.-G. Gao, H.-W. Hou and T. C. W. Mak, *Chem. - Eur. J.*, 2014, **20**, 12416.
7 S. Sharma, K. K. Chakrahari, J. Y. Saillard and C.-W. Liu, *Acc. Chem. Res.*, 2018, **51**, 2475.
8 Z.-J. Guan, F. Hu, S.-F. Yuan, Z.-A. Nan, Y.-M. Lin and Q.-M. Wang, *Chem. Sci.*, 2019, **10**, 3360.
9 E. Khatun, M. Bodiuzzaman, K. S. Sugi, P. Chakraborty, G. Paramasivam, W. A. Dar, T. Ahuja, S. Antharjanam and T. Pradeep, *ACS nano*, 2019, **13**, 5753.
10 M. Walter, J. Akola, O. Lopez-Acevedo and H. Häkkinen, *Proc. Natl. Acad. Sci. U.S.A.*, 2008, **105**, 9157.
11 H. Häkkinen, *Chem. Soc. Rev.*, 2008, **37**, 1847.
12 W. D. Knight, K. Clemenger, W. A. Heer, W. A. Saunders, M.-Y. Chou and M. L. Cohen, *Phys. Rev. Lett.*, 1984, **52**, 2141.
13 R. R. Nasaruddin, T.-K. Chen, N. Yan and J.-P. Xie, *Coord. Chem. Rev.*, 2018, **368**, 60.
14 Q.Tang, R. Ouyang, Z.-Q. Tian and D.-E. Jiang, *Nanoscale*, 2015, **7**, 2225.
15 T. Higaki, C.-J. Zeng, Y.-X. Chen, E. Hussain and R.-C. Jin, *CrystEngComm*, 2016, **18**, 6979.
16 K. Hirano, S. Takano and T. Tsukuda, *J. Phys. Chem.*, 2021, **125**, 9930.
17 S.-F. Yuan, Z.-J. Guan, W.-D. Liu and Q.-M. Wang, *Nat. Commun.*, 2019, **10**, 4032;
18 D. J. Huard, A. Demissie, D. Kim, D. Lewis,R. M. Dickson, J. T. Petty and R. L. Lieberman, *J. Am. Chem. Soc.*, 2018, **141**, 11465.
19 C. Cerretani, H. Kanazawa, T. Vosch and J. Kondo, *Angew. Chem. Int. Ed.*, 2019, **58**, 17153.
20 X. Li, Z. Huang, R. Zavala and M. L. Tang, *J. Phys. Chem. Lett.* 2016, **7**, 1955.
21 J. Van Damme and F. Du Prez, *Prog. Polym. Sci.*, 2018, **82**, 92.
22 R. G. Pearson, *J. Am. Chem. Soc.*, 1963, **85**, 3533.
23 J. A. Campbell, *J. Chem. Educ.*, 1968, **45**, 581.
24 W. P. Slichter, *J. Chem. Educ.*, 1968, **45**, 634.
25 K. Yonesato, H. Ito, H. Itakura, D. Yokogawa, T. Kikuchi, N. Mizuno, K. Yamaguchi and K. Suzuki, *J. Am. Chem. Soc.*, 2019, **141**, 19550.
26 S. Chen, W.-H. Fang, L. Zhang and J. Zhang, *Angew. Chem. Int. Ed.*, 2018, **57**, 11252.
27 K.-G. Liu, X.-M. Gao, T. Liu, M.-L. Hu and D.-E. Jiang, *J. Am. Chem. Soc.*, 2020, **142**, 16905.
28 X.-M. Luo, C.-H. Gong, X.-Y. Dong, L. Zhang and S.-Q. Zang, *Nano Res.*, 2021, **14**, 2309.
29 Z. Wang, H.-T. Sun, M. Kurmoo, Q.-Y. Liu, G.-L. Zhuang, Q.-Q. Zhao, X.-P. Wang, C.-H. Tung and D. Sun, *Chem. Sci.*, 2019, **10**, 4862.
30 A. Ahmadivand, N. Pala and D. Ö. Güney, *Opt. Express*, 2015, **23**, A682.
31 P. S. Engel, H. Wu and W. B. Smith, *Org. Lett.*, 2001, **3**, 3145.
32 E. Yousif and R. Haddad, *SpringerPlus*, 2013, **2**, 1.
33 J. Manchester, D. M. Bassani, J.-L. H. Duprey, L. Giordano, J. S. Vyle, Z.-Y. Zhao and J. H. Tucker, *J. Am. Chem. Soc.*, 2012, **134**, 10791.
34 J. V. Crivello and M. Jang, *J. Photoch. Photobio. A*, 2003, **159**, 173.
35 A. Tlahuice-Flores and A. Muñoz-Castro, *Int. J. Quantum Chem.*, 2019, **119**, e25756;
36 I. Chakraborty and T. Pradeep, *Chem. Rev.*, 2017, **117**, 8208.
37 T. T. Zhuang, Y. Liu, Y. Li, Y. Zhao, L. Wu, J. Jiang and S. H. Yu, *Angew. Chem. Int. Ed.*, 2016, **55**, 6396.
38 J. Su, N. Xu, R. Murase, Z.-M. Yang, D. M. D'Alessandro, J.-L. Zuo and J. Zhu, *Angew. Chem. Int. Ed.*, 2021, **60**, 4789.
39 G. Zhu, C. Bao, Y. Liu, X. Shen, C. Xi, Z. Xu and Z. Ji, *Nanoscale*, 2014, **6**, 11147.
40 B. Kim, H. Shin, T. Park, H. Lim and E. Kim, *Adv. Mater.*, 2013, **25**, 5483.
41 G. te Velde, F. M. Bickelhaupt, S. J. A. van Gisbergen, C. F. Guerra, E. J. Baerends, J. G. Snijders and T. Ziegler, *J. Comput. Chem.*, 2001, **22**, 931.
42 ADF2018, SCM, Theoretical Chemistry, Vrije Universiteit: Amsterdam, The Netherlands; http://www.scm.com.
43 E. Van Lenthe, E. J. Baerends and J. G. Snijders, *J. Chem. Phys.*, 1994, **101**, 9783.
44 A. D. Becke, *Phys. Rev. A*, 1988, **38**, 3098.
45 J. P. Perdew, *Phy. Rev. B*, 1986, **33**, 8822.
46 E. Van Lenthe and E. J. Baerends, *J. Comput. Chem.*, 2003, **24**, 1142.

47 S. Grimme, *J. Comput. Chem.*, 2006, **27**, 1787.
48 M. J. Frisch, G. W. Trucks, H. B. Schlegel, G. E. Scuseria, M. A. Robb, J. R. Cheeseman, G. Scalmani, V. Barone, G. A. Petersson, H. Nakatsuji, X. Li, M. Caricato, A. V. Marenich, J. Bloino, B. G. Janesko, R. Gomperts, B. Mennucci, H. P. Hratchian, J. V. Ortiz, A. F. Izmaylov, J. L. Sonnenberg, D. Williams-Young, F. Ding, F. Lipparini, F. Egidi, J. Goings, B. Peng, A. Petrone, T. Henderson, D. Ranasinghe, V. G. Zakrzewski, J. Gao, N. Rega, G. Zheng, W. Liang, M. Hada, M. Ehara, K. Toyota, R. Fukuda, J. Hasegawa, M. Ishida, T. Nakajima, Y. Honda, O. Kitao, H. Nakai, T. Vreven, K. Throssell, J. A. Jr. Montgomery, J. E. Peralta, F. Ogliaro, M. J. Bearpark, J. J. Heyd, E. N. Brothers, K. N. Kudin, V. N. Staroverov, T. A. Keith, R. Kobayashi, J. Normand, K. Raghavachari, A. P. Rendell, J. C. Burant, S. S. Iyengar, J. Tomasi, M. Cossi, J. M. Millam, M. Klene, C. Adamo, R. Cammi, J. W. Ochterski, R. L. Martin, K. Morokuma, O. Farkas, J. B. Foresman and D. J. Fox, Gaussian16, Gaussian, Inc.: Wallingford, CT, 2016.
49 E. D. Glendening, J. K. Badenhoop, A. E. Reed, J. E. Carpenter, J. A. Bohmann and C. M. Morales, Weinhold, F. NBO 6.0. Theoretical Chemistry Institute, University of Wisconsin (Madison, WI, 2001, http://nbo6.chem.wisc.edu).
50 F. Weigend and R. Ahlrichs, *Phys. Chem. Chem. Phys.*, 2005, **7**, 3297.
51 C. Adamo and V. Barone, *J. Chem. Phys.*, 1999, **110**, 6158.
52 J.-T. Wu and S. L.-C. Hsu, *J. Nanopart. Res.*, 2011, **13**, 3877.
53 P. Nalawade, P. Mukherjee and S. Kapoor, *J. Nanostruct. Chem.*, 2014, **4**, 113.
54 M. Walter, J. Akola, O. Lopez-Acevedo, P. D. Jadzinsky, G. Calero, C. J. Ackerson, R. L. Whetten, H. Grönbeck and H. Häkkinen, *Proc. Natl. Acad. Sci. U.S.A.*, 2008, **105**, 9157.
55 H. Schmidbaur and A. Schier, *Angew. Chem. Int. Ed.*, 2015, **54**, 746.
56 Z. Wang, H.-F. Su, M. Kurmoo, C.-H Tung, D. Sun and L.-S. Zheng, *Nat. Commun.*, 2018, **9**, 1.
57 J. Yan, J. Zhang, X. Chen, S. Malola, B. Zhou, E. Selenius, X. Zhang, P. Yuan, G. Deng and K. Liu, *Nati. Sci. Rev.*, 2018, **5**, 694.
58 X. Kang, S.-X. Wang, Y.-B. Song, S. Jin, G.-D. Sun, H.-Z. Yu and M.-Z. Zhu, *Angew. Chem. Int. Ed.*, 2016, **55**, 3611.
59 X. Kang, X.-W. Li, H.-Z. Yu, Y. Lv, G.-D. Sun, Y.-F. Li, S.-X. Wang and M.-Z. Zhu, *RSC Adv.*, 2017, **7**, 28606.
60 Y.-P. Xie, Y.-L. Shen, G.-X. Duan, J. Han, L.-P. Zhang and Lu, X, *Mater. Chem. Front.*, 2020, **4**, 2205.
61 J. Wang, Y. Li, L. Deng, N. Wei, Y. Weng, S. Dong, D. Qi, J. Qiu, X. Chen and T. Wu, *Adv. Mater.*, 2017, **29**, 1603730.
62 B. Lü, Y. Chen, P. Li, B. Wang, K. Müllen and M. Yin, *Nat. Commun.*, 2019, **10**, 767.
63 G. Chen, J. Sun, Q. Peng, Q. Sun, G. Wang, Y. Cai, X. Gu, Z. Shuai and B. Z. Tang, *Adv. Mater.*, 2020, **32**, 1908537.
64 C. Hua, P. W. Doheny, B. Ding, B. Chan, M. Yu, C. J. Kepert and D. M. D'Alessandro, *J. Am. Chem. Soc.*, 2018, **140**, 6622.
65 M.-Q. Li, M. Zhao, L.-Y. Bi, Y.-Q. Hu, G. Gou, J. Li and Y.-Z. Zheng, *Inorg. Chem.*, 2019, **58** , 6601.
66 S. Wang, J. Chen, J. Lin, C. Yang, F. Huang and D. Chen, *J. Mater. Chem. C*. 2019, **7**, 14571.
67 M. Gao, L. Zhu, C. K. Peh and G. W. Ho, *Energy Environ. Sci.*, 2019, **12**, 841.
68 L. Zhu, T. Ding, M. Gao, C. K. N. Peh and G. W. Ho, *Adv. Energy Mater.*, 2019, **9**, 1900250.
69 N. Selvakumar, N. Manikandanath, A. Biswas and H. C. Barshilia, *Sol. Energ. Mat. Sol. C.*, 2012, **102**, 86-92.
70 Z.-X. Yao, J.-Z. Li, H.-H. Wang, X. Cheng, L.-L. Hou, D.-N. Yu, D. Chen, W.-Y. Dan and K.-G. Liu, *Dalton Trans.*, 2022, **51**, 6053.
71 H.-H. Wang, J.-Z. Li, J. Nie, Z.-X. Yao, H.-J. Li, K.-G. Liu and X.-W. Yan, *Inorg. Chim. Acta*, 2021, **514**, 120018.
72 D.-N. Yu, Z.-X. Yao, F. Bigdeli, X.-M. Gao, X. Cheng, J.-Z. Li, J.-W. Zhang, W. Wang, Z.-J. Guan, Y.-F. Bu, K.-G. Liu and A. Morsali, *Inorg. Chem.*, 2023, **62**, 401.
73 Y.-J. Zhong, J.-H. Liao, T.-H. Chiu, S. Kahlal, C.-J. Lin, J.-Y. Saillard and C.-W. Liu, *Angew. Chem. Int. Ed.*, 2021, **60**, 12712.
74 *H.-Y. Yang, J. Lei, B.-H. Wu, Y. Wang, M. Zhou, A.-D. Xia, L.-S. Zheng and N.-F. Zheng, *Chem. Commun.*, 2013, **49**, 300.
75 Z.-Y. Wang, M.-Q. Wang, Y.-L. Li, P. Luo, T.-T. Jia, R.-W. Huang, S.-Q. Zang and T. C. W. Mak, *J. Am. Chem. Soc.*, 2018, **140**, 1069.
76 Y. Kikukawa, Y. Kuroda, K. Suzuki, M. Hibino, K. Yamaguchi and N. Mizuno, *Chem. Commun.*, 2013, **49**, 376.
77 Z. Wang, H.-F. Su, M. Kurmoo, C.-H. Tung, D. Sun and L.-S. Zheng, *Nat. Commun.*, 2018, **9**, 2094.
78 Z. Wang, F.-L. Yang, Y. Yang, Q.-Y. Liu and D. Sun, *Chem. Commun.*, 2019, **55**, 10296.
79 Z. Wang, Q.-P. Qu, H.-F. Su, P. Huang, R. K. Gupta, Q.-Y. Liu, C.-H. Tung, D. Sun and L.-S. Zheng, *Sci. China Chem.*, 2020, **63**, 16.
80 S.-F. Yuan, P. Li, Q. Tang, X.-K. Wan, Z.-A. Nan, D.-E. Jiang, and Q.-M. Wang, *Nanoscale*, 2017, **9**, 11405.
81 H.-Y. Yang, Y. Wang and N.-F. Zheng, *Nanoscale*, 2013, **5**, 2674.
82 K. Yonesato, H. Ito, D. Yokogawa, K. Yamaguchi, K. Suzuki, *Angew. Chem. Int. Ed.*, 2020, **59**, 16361.